Journal of Energy Storage 31 (2020) 101489

Contents lists available at ScienceDirect

Journal of Energy Storage

journal homepage: www.elsevier.com/locate/est

Implementation of generative adversarial network-CLS combined with bidirectional long short-term memory for lithium-ion battery state prediction

Haoliang Zhang[a], Wei Tang[b], Woonki Na[c], Pyeong-Yeon Lee[d], Jonghoon Kim[d,*]

[a] The University of Oklahoma, Norman, OK 73019, USA
[b] College of Electrical and Information Engineering, Shaanxi University of Science & Technology, Xi'an, Shaanxi, 710021, China
[c] Department of Electrical and Computer Engineering, California State University, Fresno, CA 93740-8030, USA
[d] Energy Storage and Conversion Laboratory, Department of Electrical Engineering, Chungnam National University, Daejeon 34134, Republic of Korea

ARTICLE INFO

Keywords:
Battery state prediction
Generative adversarial network-CLS
Bidirectional-long short-term memory
Recurrent neural network
State-of-charge

ABSTRACT

This study newly introduces a complementary cooperative algorithm considering generative adversarial network (GAN)-Conditional Latent Space (CLS) combined with bidirectional long short-term memory (BLSTM) for improved and efficient lithium-ion rechargeable battery state prediction. The GAN-CLS algorithm, which is an advanced method of GAN, can generate corresponding images from an input label description. Long short-term memory (LSTM) is a specific recurrent neural network (RNN) architecture that can predict sequences more accurately than conventional RNNs. In terms of battery state prediction, the combination of two methods (GAN-CLS and LSTM) surely provides more improved and efficient rechargeable battery state prediction in contrast to conventional state predictors. The procedure of this study is as follows. First, we propose methods to enhance the data from battery charge/discharge by converting prepared data to images; then, the GAN-CLS method is used to generate corresponding battery data from previous images. Subsequently, the generated data is used to train the BLSTM model. Finally, the trained model is used to predict the battery state. By various experiments and verification, it is concluded that the proposed study can be a good solution for rechargeable battery state prediction (reduction of the time cost 50 times in modeling and 20 times in train/test, provision of a more accurate prediction mean square error (MSE) smaller than 0.0025 and the average MSE less than 0.0013).

1. Introduction

The state-of-charge (SOC) of the lithium-ion (Li-ion) battery is an important evaluation index of a battery management system (BMS). Therefore, performing an accurate measurement of the SOC is the main concern in analyzing battery-pack performance. In general, the battery pack is composed of hundreds and thousands of single cells for high voltage and energy storage [1]. The characteristics of batteries are different after undergoing several charge/discharge cycles. The BMS test needs to be executed many times for desired model accuracy, even though the characteristics of batteries are slightly different under the same state-of health (SOH).

Coulomb counting is the basic method to measure SOC. In this method, the current is integrated over time, and the integral is divided by the capacity to obtain the SOC [2,3]. However, Coulomb counting methods highly depend on the initial SOC estimation and the bias in the current sensing. The conventional SOC estimation algorithm is represented by a Kalman filter [4,5]; however, the SOC-open circuit voltage (OCV) characteristics of a battery have strong nonlinearity at the beginning and end of the charge/discharge state [6–8]. The extended Kalman filter (EKF) [9–12] is proposed to deal with the problem of predicting the SOC under the linear assumption of the Kalman filter. However, the performance of the Kalman filter and its derivative version depends on an accurate battery model, such as the conventional Thevenin model or second Thevenin model [13]. Both models require offline parameter identification, as well as measurement of the OCV, and a determination of the time elapsed of the model. Jian Chen et al. [14,15] proposed the use of the adaptive neuro-fuzzy and radial basis function neural network as a nonlinear observer. In the experiment of [14], the battery is discharged with a constant current in steps of 5% of capacity and rested; then, the corresponding resistance R can be calculated as the ratio of the instantaneous voltage drop U and current I. Then, the parameters of the RC networks at the corresponding measured SOCs can be determined. Finally, the neural network is used to fit

* Corresponding author.
E-mail address: qwzxas@hanmail.net (J. Kim).

https://doi.org/10.1016/j.est.2020.101489
Received 24 July 2019; Received in revised form 23 April 2020; Accepted 25 April 2020
Available online 20 June 2020

Nomenclature

GAN	generative adversarial network
CLS	conditional latent space
LSTM	long short-term memory
RNN	recurrent neural network
BLSTM	bidirectional-long short-term memory
SOC	state-of-charge
BMS	battery management system
SOH	state-of-health
OCV	open circuit voltage
GA	genetic algorithm
EKF	extended Kalman filter
RBF	radial basis function
RSMO	robust sliding-mode observer
ANN	artificial neural network
BPNN	back propagation neural network
CNN	convolutional neural network
PCC	Pearson's correlation coefficient
CCD	constant current discharge
MSE	mean square error
D	discriminator network in the GAN
G	generator network in the GAN
z	low-dimension noise vector in the GAN
L	likelihood function
KL	Kullback-Leibler divergence
G	optimization generator in the GAN
JS	Jensen-Shannon divergence
x_t	input state (input x in time t) in the LSTM
c_t	cell state in the LSTM
$\tilde{c}_t$	temporal cell state in the LSTM
h_t	hidden state in the LSTM
f_t	forget gate in the LSTM
i_t	memory gate in the LSTM
o_t	output gate in the LSTM
m_t	memory cell outputs in the LSTM
y_t	output state (output y in time t) in the LSTM
σ	sigmoid function in the LSTM
b_i	bias vector of input gate in the LSTM
b_f	bias vector of forget gate in the LSTM
b_c	bias vector of cell activation vectors in the LSTM
b_o	bias vector of output gate in the LSTM
b_y	bias vector of output state in the LSTM
$\odot$	element-wise product of the vector in the LSTM
ϕ	output activation function in the LSTM
W_{ix}	weight matrix from input state x to the input gate i in the LSTM
W_{im}	weight matrix from memory cell output m to the input gate i in the LSTM
W_{ic}	weight matrix from cell state c to the input gate i in the LSTM
W_{fx}	weight matrix from input state x to the forget gate f in the LSTM
W_{fm}	weight matrix from memory cell output m to the forget gate f in the LSTM
W_{fc}	weight matrix from cell state c to the forget gate f in the LSTM
W_{cx}	weight matrix from input state x to the cell state c in the LSTM
W_{cm}	weight matrix from memory cell output m to the cell state c in the LSTM
W_{ox}	weight matrix from input state x to the output gate o in the LSTM
W_{om}	weight matrix from memory cell output m to the output gate o in the LSTM
W_{oc}	weight matrix from cell state c to the output gate o in the LSTM
W_{ym}	weight matrix from memory cell output m to the output state y in the LSTM

the curve, and the Thevenin model is used to estimate the SOC. This method can yield an accurate estimation if the battery has the same SOH. Han et al. [16] used the genetic algorithm (GA) to identify the battery capacity and analyze the battery age model under different test temperatures. In [17], a radial basis function (RBF) neural network (NN) was used to learn the bounds of the uncertain dynamics of the battery equivalent circuit model. Then, the outputs of the RBF NN were used to estimate the SOC based on a robust sliding-mode observer (RSMO). However, this requires tremendous testing under different temperatures to identify the model parameters. Other SOC estimation methods are established on machine learning strategies, which encompass artificial neural networks (ANNs), fuzzy NNs, back propagation neural networks (BPNNs), and adaptive fuzzy NNs [18–22]. These data-oriented approaches treat the battery model as a black box, with requiring knowledge of the battery internal structure. The battery model is treated in the weights of NNs. A large amount of experimental data is required to train the NNs for high accuracy. In addition, it is difficult to balance the model precision and generalization performance. Furthermore, it necessitates tremendous computing workload and resource consumption. A summary of the lithium-ion battery state prediction methods is listed in Table 1.

In this study, a method involving the use of GAN-CLS (called as matching-aware discriminator) to generate the required data, rather than running experiments, is adopted [23]. In this method, measured data with different SOH are padded with zeros at the end, such that all data are of the same length. Then, the vectors are reshaped as 2-dimensional images, and convolutional neural network (CNN) is used to extract the rough and detailed features as needed. For the original GAN, the random data with fixed distribution were used to generate the desired distribution. However, battery SOC-OCV characteristics vary with different SOH, which means that the SOC-OCV characteristics exhibit a different distribution. In the GAN-CLS model, the discriminator in GAN receives the generated data and corresponding SOH, such that the input data includes the corresponding SOH information. The performance of

Table 1
A summary of the lithium-ion battery state prediction methods.

Methods	Advantages	Disadvantages
Coulomb counting	Easy implementation	- Inaccuracy due to error accumulation - Dependency on the initial SOC values
Kalman filter, extended Kalman filter	Accuracy	- High computational cost - Needs identification of model parameters
Fuzzy neural network	No model needed	- Needs of large amount of data
Genetic algorithm	Accuracy	- Very high computational load
Sliding model observer	Accuracy, Robustness	- Nonlinear, hard implementation

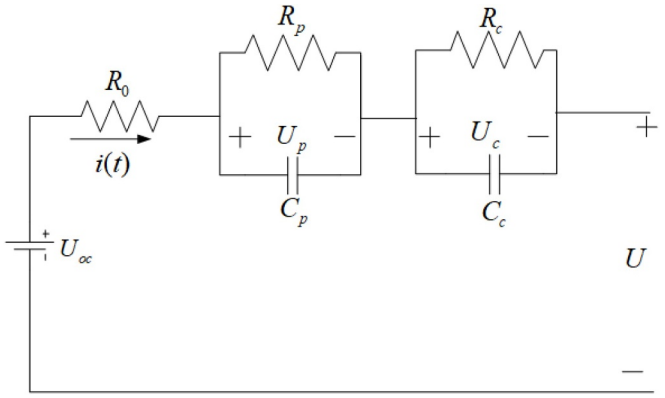

Fig. 1. Structure of Thevenin model (one resistance and two RC-ladders).

the generated data was tested based on a significance test, using the best data to represent the experimental data. The generated data are used to train the bidirectional-LSTM (BLSTM) networks that operate on the input sequence in both directions to facilitate optimal decision-making for the current input [24,25]. As a result, the GAN-CLS generates high-quality pseudo-experimental data, which can be used for BMS or fault-detection simulation. The proposed methods reduce the time cost 50 times in modeling and 20 times in train/test. The results show a predicted mean square error (MSE) smaller than 0.002. The proposed methods significantly reduce the time and resource cost.

2. Battery model and network architectures

2.1. Conventional battery model

Equivalent-circuit models of battery cells are widely used in SOC estimation. Among these models, Fig. 1 shows the improved Thevenin model. Eqs. (1) through (3) represents the mathematical expressions of the second order model [26].

$$\frac{dU_p(t)}{dt} = -\frac{U_p(t)}{R_p C_{pa}} + i_L(t)/C_p \tag{1}$$

$$\frac{dU_c(t)}{dt} = -\frac{U_c(t)}{R_c C_c} + i_L(t)/C_c \tag{2}$$

$$U(t) = U_{oc}(t) - R_o i_L(t) - U_p(t) - U_c(t) \tag{3}$$

Thevenin model has the polarization resistance R_p and polarization capacitor C_p, U_p is voltage on capacitance C_p, $i(t)$ is charge/discharge current. C_c and R_c are concentration polarization capacitance and

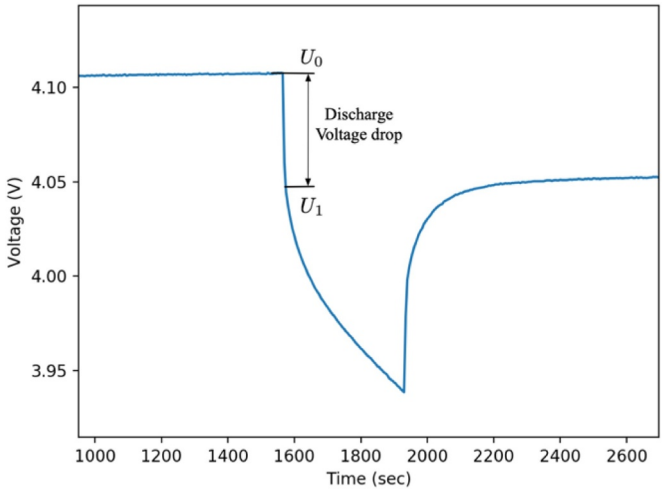

Fig. 2. Experimental voltage drop with a pulse current and its definition.

concentration polarization resistance, U_{oc} is open circuit voltage, U_{pa} is defined as voltage on capacitance C_{pa}, $i_L(t)/U_L$ are the charge/discharge current and terminal voltage. Assuming $\frac{dU_{oc}(t)}{dt} \approx 0$, taking time the derivative of $U_L(t)$ gives

$$\frac{dU_L(t)}{dt} = -\frac{1}{R_{pc}C_{pc}}U_L(t) + \left[\frac{1}{R_{pa}C_{pa}} - \frac{1}{R_{pc}C_{pc}}\right]U_{pa}(t) - \left[\frac{R_o}{R_{pc}C_{pc}} + \frac{1}{C_{pc}} + \frac{1}{C_{pa}}\right]i_L(t) + \frac{1}{R_{pc}C_{pc}}U_{oc} - R_o\frac{di_L(t)}{dt} \tag{4}$$

The EKF algorithm can be employed for SOC estimation based on above circuit model. But, it strongly depends on the accuracy of the battery model parameters. Generally, in order to acquire experimental data for an identification of the model parameters, the pulse power characterization test (HPPC) has been conducted. Fig. 2 shows the terminal voltage response of the battery during the HPPC test at SOC 95%. As displayed in Fig. 2, when a pulse discharge current is applied, a voltage drop defined as $\Delta U = |U_1 - U_0|$, has appeared. Then, the resistance R_0 can be given by $R_0 = \Delta U/i(t)$ and other parameters can be similarly obtained. Unfortunately, it is very infeasible in practical application. According to different operational conditions such as temperature and aging, it is not easy to sustain a good battery performance.

Fig. 3 shows two examples of varied battery electrical characteristics under different temperature effect, especially low (0°C) and high (50°C), then all different voltage curves are easily checked. According to varied electrical characteristics caused by temperature and aging

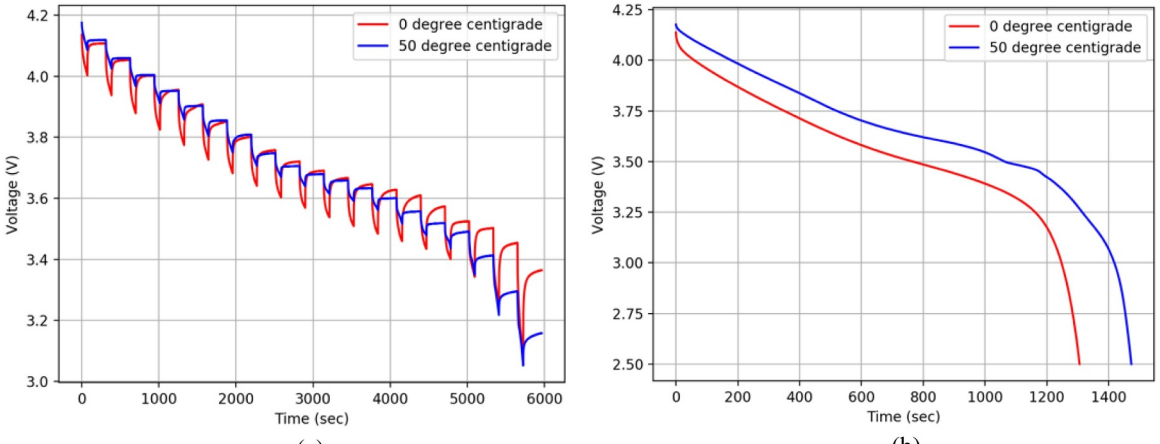

Fig. 3. Voltage comparison of battery electrical characteristics varied by low (0°C) and high (50°C) temperature effects. (a) For OCV, (b) For discharge capacity.

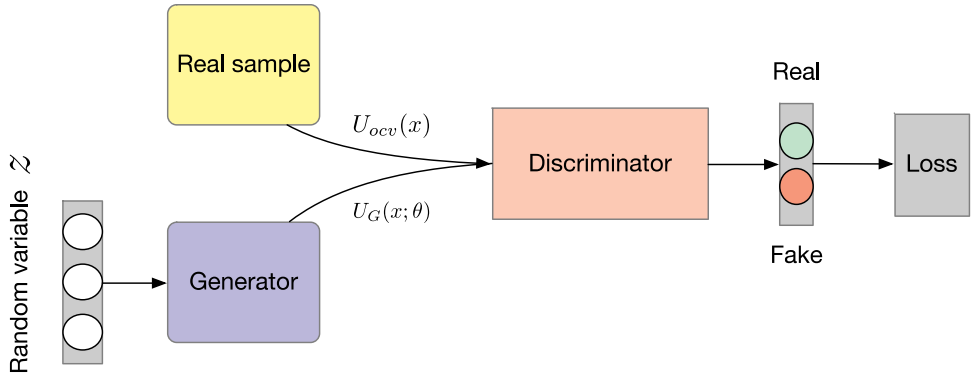

Fig. 4. Generative adversarial networks (GAN) architecture.

effects, it is surely inevitable that more increased parameter combinations should be used for SOC estimation, e.g. 2500 parameter relations in model due to different 50 temperature and 50 aging conditions. This makes the EKF empirically impossible and inefficient.

2.2. Generative adversarial networks (GAN)

The generative adversarial network scheme was proposed by Goodfellow in 2014 [27]. It consists of a discriminator network *D* and a generator network *G*. The goal of generator *G* is to maximize the probability of *D* making a mistake, and the goal of training discriminator *D* is to maximize the probability of distinguishing the generator images. The input of the generator is random data *z* from a fixed distribution, such as a Gaussian distribution, and the output of generator is the same distribution of real samples. The inputs of the discriminator are real and generator data, and the output is a value in (0, 1). The two networks compete during training; GANs are designed to reach Nash equilibrium, which means that the probability of the discriminator making a mistake is 50%.

Fig. 4 shows the GAN architecture. The generator creates a high-dimension distribution of samples based on the low-dimension noise vector *z*. This means that the sample features are included in vector *z*. Assuming a battery charge or discharge with constant current, the distribution of measured data can be represented as $U_{ocv}(x)$. The goal is to train a generator, which can create distribution $U_G(x;\theta)U_G(x;\theta)$ based on the random input vector, with the target θ calculated by likelihood function *L*,

$$L = \prod_{i=1}^{m} U_G(x^i;\theta) \tag{5}$$

where x^i is the ith sample from the real measured characteristic point. The maximum likelihood estimation of θ is given by

$$\theta^* = \arg\max_{\theta} \prod_{i=1}^{m} U_G(x^i;\theta) \Leftrightarrow \arg\max_{\theta} \log \prod_{i=1}^{m} U_G(x^i;\theta) \tag{6}$$

$$= \arg\max_{\theta} \prod_{i=1}^{m} \log U_G(x^i;\theta) \approx \arg\max_{\theta} E_{x\sim U_{ocv}}[\log U_G(x;\theta)] \tag{7}$$

There is no change that subtract $\int_x U_{ocv}(x)\log U_{ocv}(x)dx$ $\int_x U_{ocv}(x)\log U_{ocv}(x)dx$. $U_{ocv}(x)\log U_{ocv}(x)dx$ from Eq. (6), because it is equal to a constant value.

$$\Leftrightarrow \arg\max_{\theta} \int_x U_{ocv}(x)\log U_G(x;\theta)dx - \int_x U_{ocv}(x)\log U_{ocv}(x)dx$$
$$= \arg\max_{\theta} \int_x U_{ocv}(x)\log\frac{U_G(x:\theta)}{U_{ocv}(x)}dx = \arg\min_{\theta} KL(U_{ocv}(x)\|U_G(x;\theta)) \tag{8}$$

where KL is the Kullback-Leibler divergence [28].

$$U_G(x) = \int_x U_{prior}(z) I_{[U_z=x]}dz \tag{9}$$

$$I_{G(z)} = \begin{cases} 0 & U(z) \neq x \\ 1 & U(z) = x \end{cases} \tag{10}$$

The $U_{prior}(z)$ is a prior distribution, the generated distribution is $U_z(z)$, D is defined as a function that measures the difference between the $U_z(z)$ and $U_{ocv}(x)$, and the function V is given by

$$V(G,D) = E_{x\sim U_{ocv}(x)}[\log D(X)] + E_{z\sim U_z(z)}[\log(1 - D(G(z)))] \tag{11}$$

The optimization generator model G* is given by

$$G^* = \arg\min_G \max_D V(G,D) \tag{12}$$

The objective function is

$$\min_G \max_D V(G,D) = E_{x\sim U_{ocv}(x)}[\log D(X)] + E_{z\sim U_z(z)}[\log(1 - D(G(z)))] \tag{13}$$

Eq. (12) can be treated as two functions: First, we consider the optimal discriminator D for any given generator G. Then, optimal generator G for a given random vector z is expressed as

$$\max_D V(G,D) = E_{x\sim U_{ocv}(x)}[\log D(X)] + E_{z\sim U_z(z)}[\log(1 - D(G(z)))] \tag{14}$$

$$\min_G V(G,D) = E_{z\sim U_z(z)}[\log(1 - D(G(z)))] \tag{15}$$

2.3. Conventional long short-term memory (LSTM)

Recurrent neural networks (RNN) is a method in modeling sequential data, particularly in the case of a subset of sequential data—time-series data. Fig. 5 shows the RNN architecture, where *A* represent the networks, x_t is the input *x* in time *t*, h_t $h_t$is the output of the networks, the weights of networks are tuned by backpropagation through time. RNN can well solve problems such as sentimental analysis, key term extraction, speech recognition, and machine translation; however, the RNN structure has some drawbacks, such as vanishing gradient and exploding gradient. LSTMs were first introduced to overcome the vanishing and exploding gradient problems [29]. The building block of an LSTM is a memory cell. The values associated with the

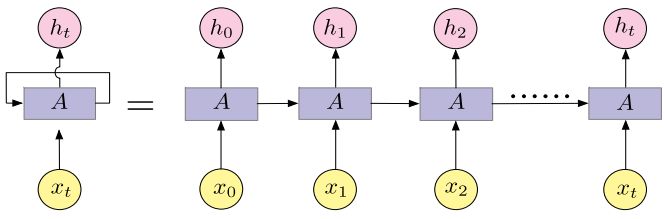

Fig. 5. Recurrent neural network (RNN) architecture.

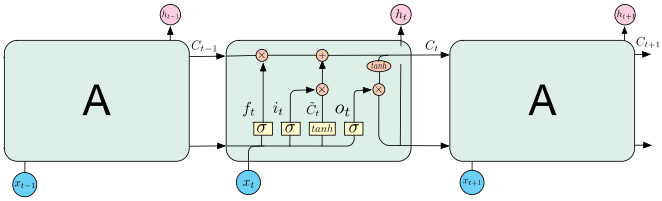

Fig. 6. Long short-term memory (LSTM) architecture.

recurrent edge is called a cell state. The LSTM is one category of RNN, which contains input x_tX$_t$, cell state c_t, temporal cell state $\tilde{c}_t$, hidden state h_t h$_t$in recurrent hidden layer, forget gate f_t, memory gate i_t, memory cell output m_t, and output gate o_t.

Fig. 6 shows the unfolded structure of a modern LSTM architecture. The compact forms of the equations for the forward pass of an LSTM unit with a forget gate are as follows.

Input gate i_t is responsible for updating the cell state as

$$i_t = \sigma(W_{ix}x_t + W_{im}m_{t-1} + W_{ic}c_{t-1} + b_i) \tag{16}$$

Forget gate f_t f$_t$allows the memory cell to reset the cell state, deciding which information is allowed to pass through or suppress. It is computed as Eq. (16), and the cell state at time t is computed in Eq. (17). Output gate o_t O$_t$decides how to update the values of hidden units.

$$f_t = \sigma(W_{fx}x_t + W_{fm}m_{t-1} + W_{fc}c_{t-1} + b_f) \tag{17}$$

$$c_t = f_t \odot c_{t-1} + i_t \odot g(W_{cx}x_t + W_{cm}m_{t-1} + b_c) \tag{18}$$

$$o_t = \sigma(W_{ox}x_t + W_{om}m_{t-1} + W_{oc}c_t + b_o) \tag{19}$$

$$m_t = o_t \odot h(c_t) \tag{20}$$

$$y_t = \phi(W_{ym}m_t + b_y) \tag{21}$$

where the W terms denote weight matrices, W_{ic}, W_{fc}, W_{oc} are diagonal weight matrices for peephole connections, σ is the sigmoid function, b bdenotes the bias vector, ⊙⊙ is the element-wise product of the vectors, ϕ is the output activation function. In addition, activation of cell inputting and outputting are used as g and h respectively.

3. Methods

3.1. Advanced generative adversarial networks (GAN)-conditional latent space (CLS)

To solve the problem that the GAN cannot create the data corresponding to the label, the auxiliary classifier GAN (AC-GAN) is proposed. Fig. 7 shows the GAN-CLS architecture, which is similar to AC-GAN, whereby the discriminator receives the generated data and corresponding information (additional parameters such as SOH, temperature, charge cycles and shocks) instead of only the generated data. The SOC-OCV characteristics have a different distribution under different SOH, thus, in this experiment, SOH and charge cycles added to both the discriminator and generator models to make the discriminator be matching-aware, which means that the discriminator can judge between the corresponding information and the x distribution.

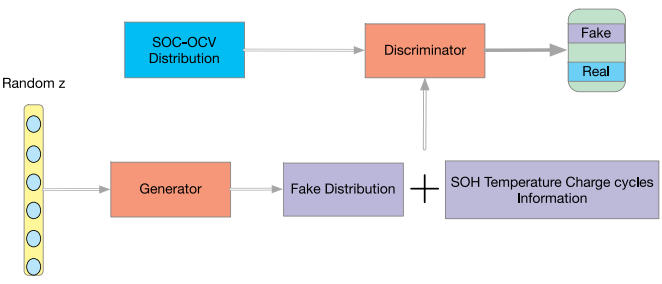

Fig. 7. Generative adversarial networks (GAN)-Conditional latent space (CLS) architecture.

The objective function of GAN is modified as:

$$V(G,D) = \frac{1}{2}\left\{\begin{array}{l} E_{(x,h)\sim U_{Ocv}(x,h)}[\log D(x,h)] + E_{z\sim U_Z(z),h\sim U_{Ocv}(h)} \\ [\log(1 - D(G(z,h)),h)] + E_{(x,h)\sim U^*_{Ocv}(x,h)}[\log(1 - D(x,h)) + \log \\ (D(x,h))] \end{array}\right\} \tag{22}$$

where h is the embedding of the SOH and charge cycles, and $U_{ocv}(x, h)$ is the distribution density function of the samples from the OCV, in which x and h are matched. $U^*_{ocv}(x, h)$ is the distribution density function of the samples from OCV consisting of SOH and OCV with mismatched corresponding information.

There is one last problem that needs to be solved: The Nash equilibrium, assumed in GAN networks, is an ideal state that does not occur in the real training process. If the discriminator is over-trained, the generator cannot learn the effective gradient, and vice-versa. Changing the original generator loss yields

$$E_{z\sim U_z(z)}[\log(1 - D(G(z)))] \rightarrow E_{z\sim U_z(z)}[-\log(1 - D(G(z)))] \tag{23}$$

The goal is to minimize the loss function

$$KL(U_{ocv}(x)\|U_G(x;\theta)) - 2JS(U_{ocv}(x)\|U_G(x;\theta)) \tag{23}$$

where JS is the Jensen-Shannon divergence. For reference, there are three changes to Wasserstein Generative Adversarial Networks (WGAN) structures [30].

① The *sigmoid* activation is removed from the last layer of the discriminator
② The *log* operation is removed from both the generator and discriminator loss function
③ A gradient penalty or clipping methods are used when the discriminator parameters are updated.

3.2. Bidirectional-long short-term memory (BLSTM)

Fig. 8 shows the BLSTM architecture, it consists of the forward LSTM layer and the backward layer, which can predict data with past and current information. It utilizes two-time direction, in which input data from the past and future of the current time frame can be used. In the LSTM structure, the information flows from the backward layer to the forward layer. On the contrary, in BLSTM, information flows from the backward layer to the forward layer and from the forward layer to the backward layer, using hidden states. For the processing of battery charge/discharge, the accurate SOC depends on past conditions, similar to the LSTM.

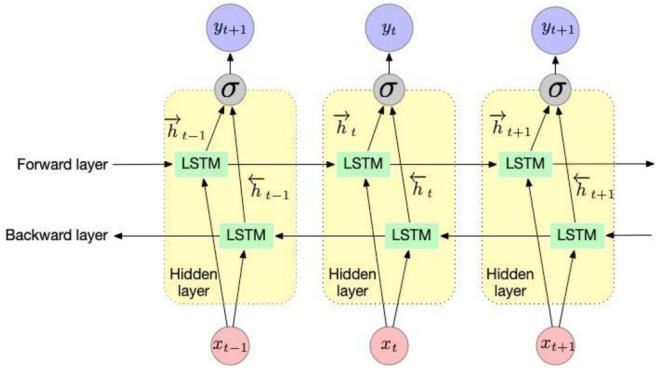

Fig. 8. Bidirectional-long short-term memory (BLSTM) architecture.

Fig. 9. Experimental equipment for proposed approach.

4. Experiments and verification

4.1. Test bench description

This approach used LG Chem. middle-power 18650-HE4 cylindrical lithium-ion batteries that has a rated capacity of 2.5Ah for experiments. Compared to the rated capacity (2.5Ah) and its nominal C-rate (1C = 2.5A), this battery has more maximum discharge current (20A, 8C-rate). Namely, because of middle-power/energy characteristics, the cathode material of this battery is basically $NiMnCoO_2$ (NMC). For reference, according to the three different ratios of Ni:Mn:Co, it is possible to produce various NMC batteries (Ni:Mn:Co = 5:2:3, 6:2:2, and 8:1:1). In case of the 18650-HE4 battery, conventional NMC (not Ni rich) is used (Ni:Mn:Co = 5:2:3). A few of the batteries are used as seeds for the GAN to learn the battery-state distribution. Fig. 9 shows experimental equipment that include a thermal chamber and test bench. The lithium-ion battery has a nominal capacity of 2.5Ah. In the test, the maximum charging voltage is set to 4.2V, and the cutoff voltage is set to 2.5V. The test is carried out in a thermal chamber, which avoids the temperature effect during the charge-discharge cycles. The discharging and charging current of 1.25A applied to the battery has slight fluctuation. The battery's terminal voltage, current, and SOC states are recorded every 5s (0.2Hz sample rate).

4.2. Experimental rechargeable battery data processing

Generating reliable and effective battery data is the key factor to obtaining highly credible simulation results. Therefore, the different battery state is used to analyze precision under different operating conditions. Fig. 10 shows a comparison of the estimated terminal voltages of nine cells under the same operating conditions. The voltage exhibits only a slight difference when the cells are under same SOH. The cells discharge at an SOC interval of 5%, and the corresponding current is shown in Fig. 11. Figs. 10 and 12 show large errors at the beginning and approaching the end of discharge, particularly at the end of discharge.

To use the proposed GAN-CLS networks, the battery state data must be reshaped to 2-D images. Then, the different filter sizes are used to extract the rough and detailed feature, and the extracted feature and its corresponding SOH are combined as input data for the discriminator, such that the matching-aware discriminator can be obtained. Figs. 13 and 14 show the battery discharge characteristics (OCV-SOC and pulse power characterization respectively), and corresponding color and gray images.

4.3. Experimental verification and discussion

The network is trained under 10 generators for each discriminator. Fig. 15 shows the generated images at different epochs; SOC-OCV use

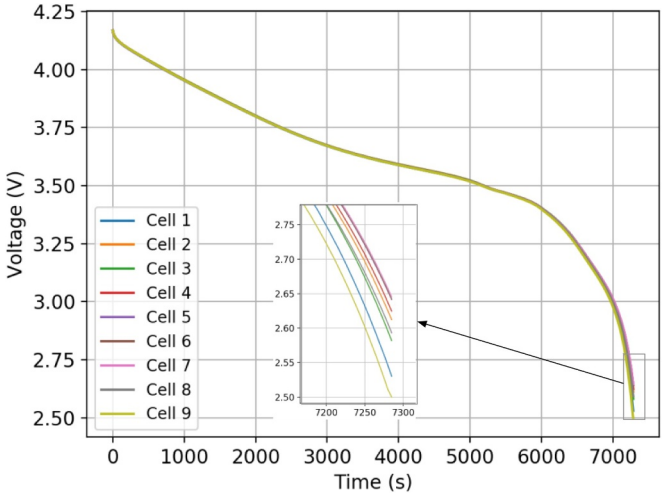

Fig. 10. Results of constant current discharge (CCD) test of nine rechargeable cells.

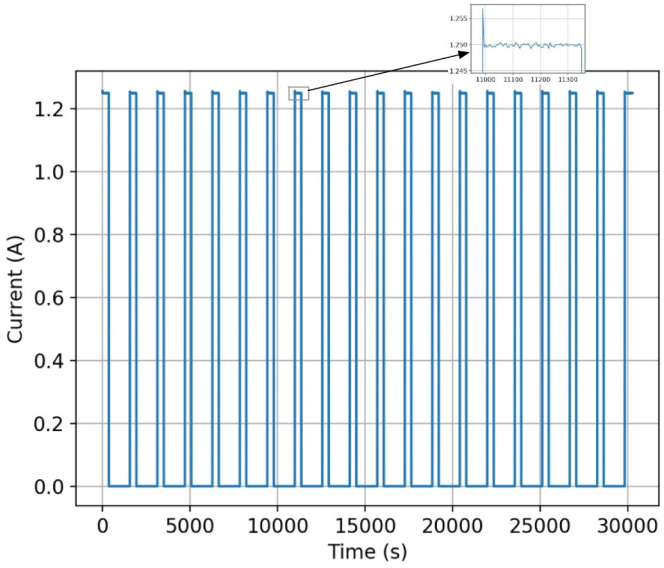

Fig. 11. Charge/discharge current for pulse power characterization test.

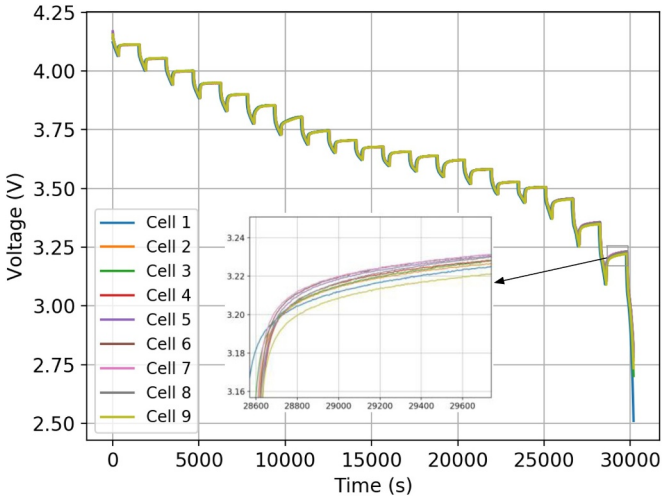

Fig. 12. Results of pulse power characterization test of nine rechargeable cells.

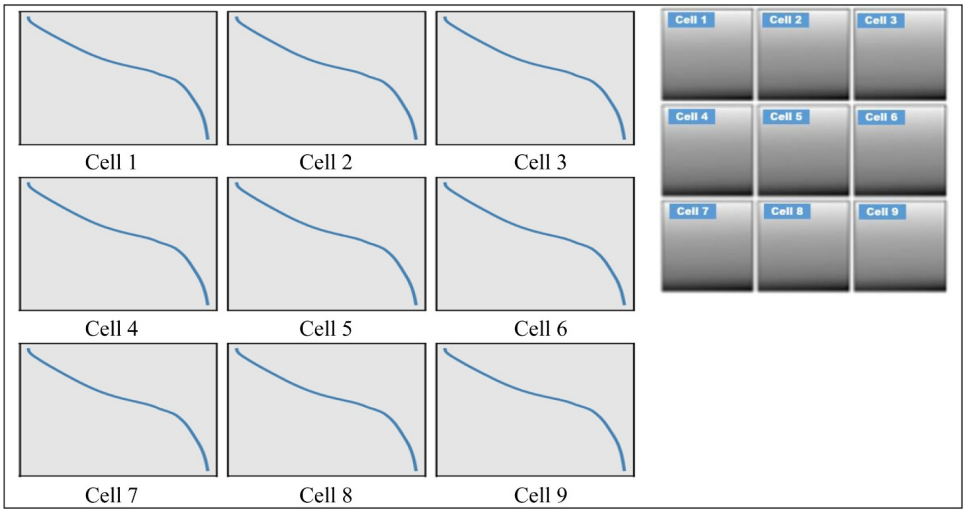

Fig. 13. SOC-OCV images of nine rechargeable batteries.

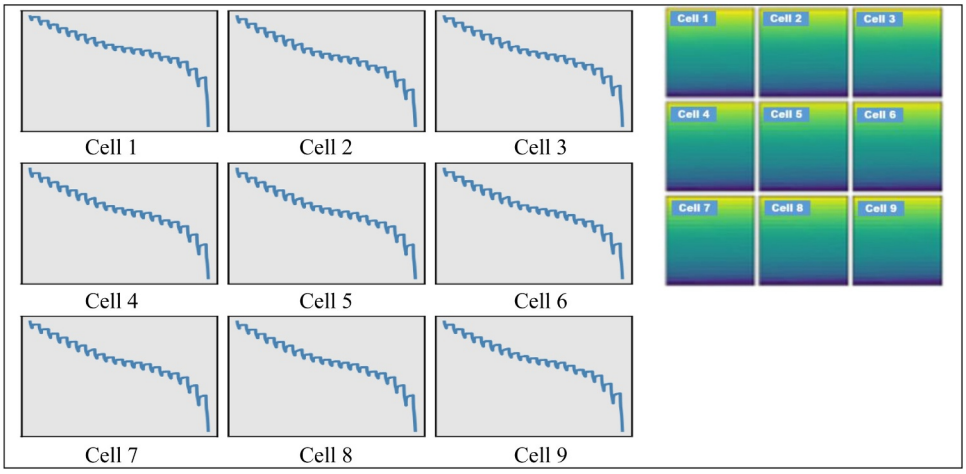

Fig. 14. Pulse power characterization images of nine rechargeable batteries.

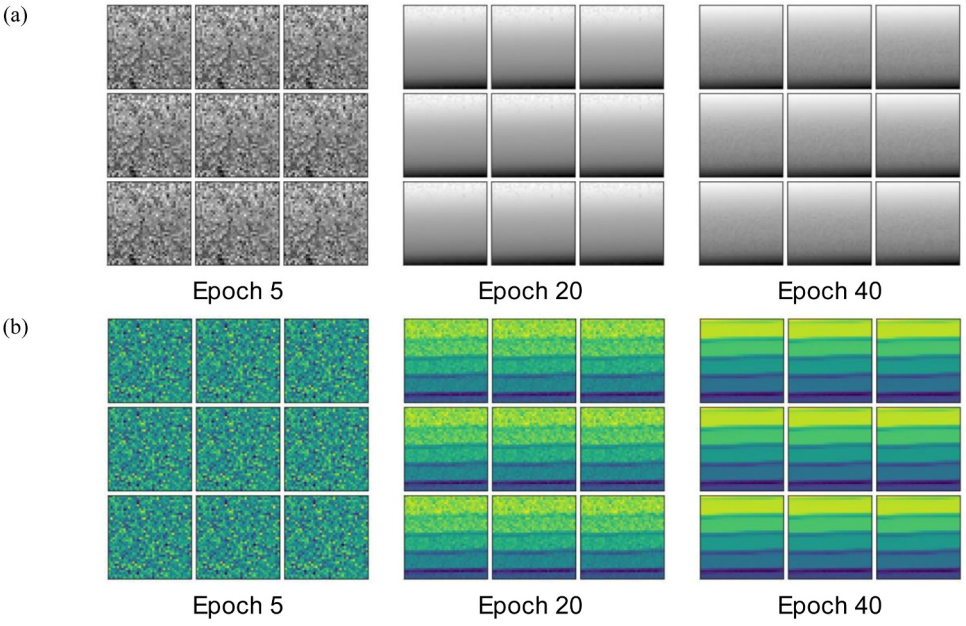

Fig. 15. Generated images of nine rechargeable batteries at three epochs (5, 20, and 40): (a) SOC-OCV, (b) Pulse power characterization.

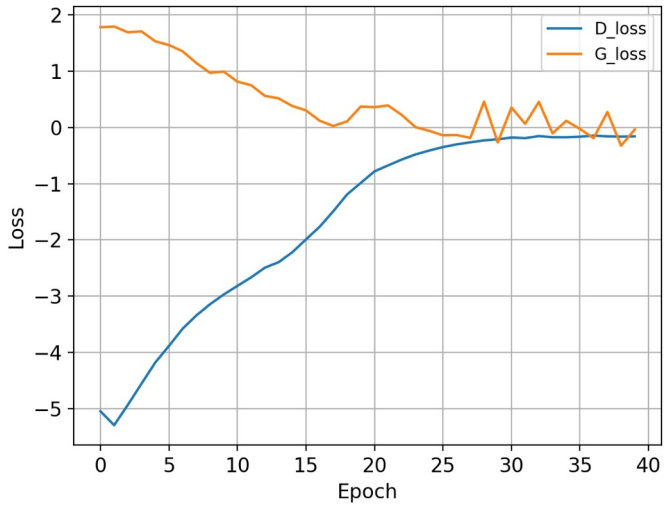

Fig. 16. Loss comparison between generator *G* and discriminator *D* which both converge to 0.

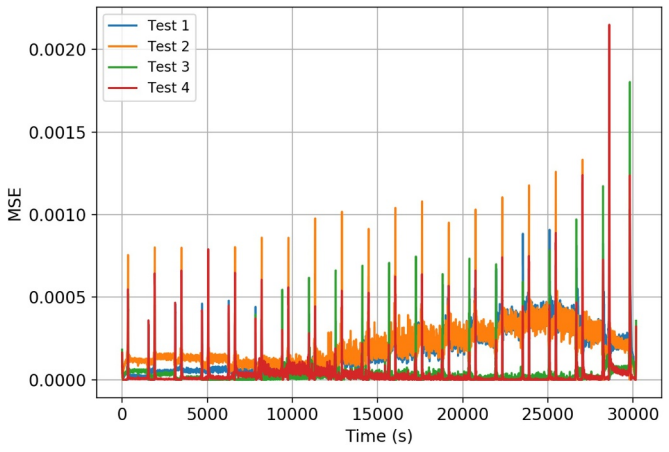

Fig. 17. Mean square error (MSE) prediction of nine rechargeable cells with different SOH.

Table 2
Average time elapsed of 10 generated datasets in each epoch.

Epoch	1	2	3	4	5	6
Time(s)	4.8627	4.7005	4.7529	4.7730	4.7369	4.7044

Table 3
Comparison of the reliability and validity performance (Error mean, MSE and PCC) of six rechargeable cells.

Cell	1	2	3	4	5	6
Error mean	-0.0976	0.0030	-0.0242	0.0298	0.0321	0.0193
MSE	0.0112	0.0000	0.0007	0.0009	0.0010	0.0003
PCC	0.9967	0.9999	0.9995	0.9997	0.9997	0.9998

gray color and pulse power characterization use color; the results are relatively poor for the pulse power characterization test cases. The algorithms generate images that match the SOH, but small layers for the pulse power characterization are exhibited in the GAN-CLS algorithm due to the more complex distribution.

Fig. 16 shows the loss of generator and discriminator which both converge to 0, the generator has slight jitter. Using the generated battery information (including terminal voltage, current, SOH, and cycles)

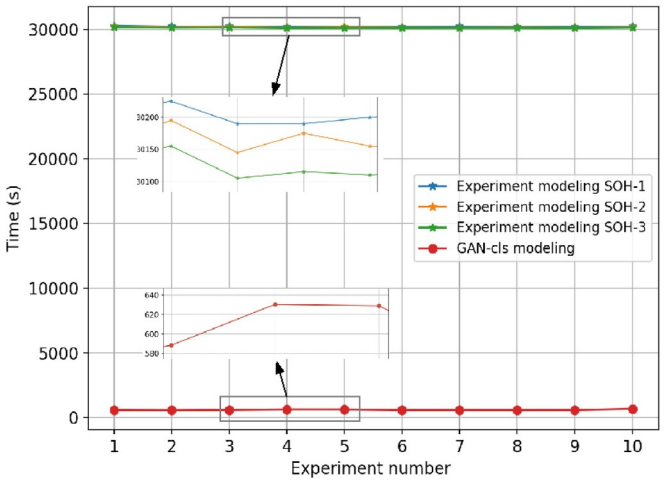

Fig. 18. Comparison between experimental modeling and GAN-CLS modeling.

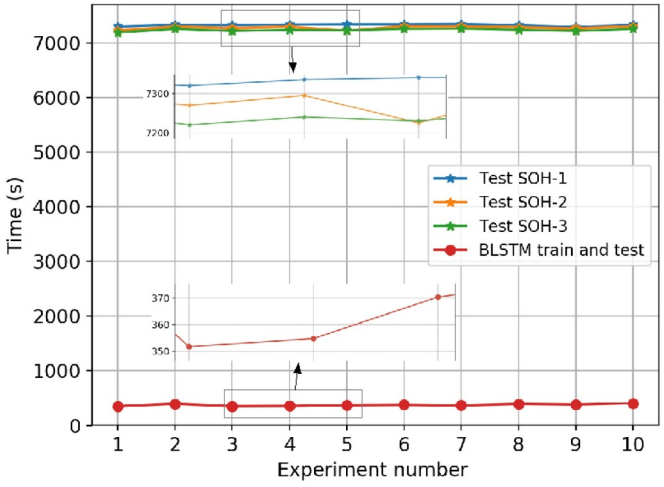

Fig. 19. Comparison between the EKF and BLSTM train test time.

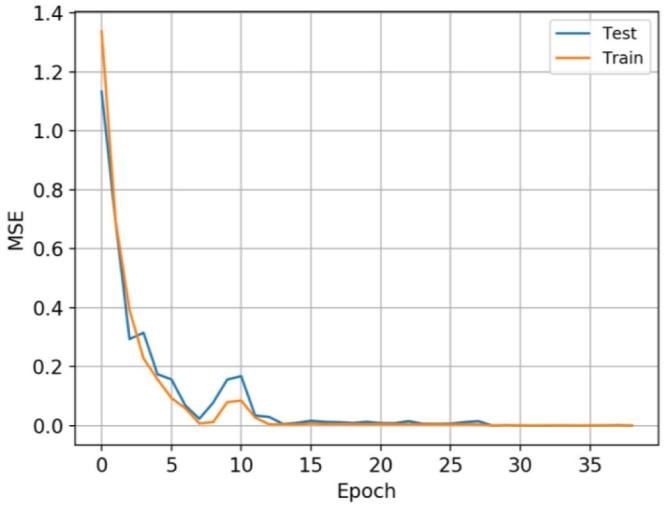

Fig. 20. Comparison of the MSE between experimental test and training in each epoch.

to train the BLSTM, the trained networks are then used to predict the experimental data. Fig. 17 shows the prediction error in 9 random cells with different SOH. The results show a predicted MSE smaller than $\pm$ 0.002 $\pm$ 0.002.

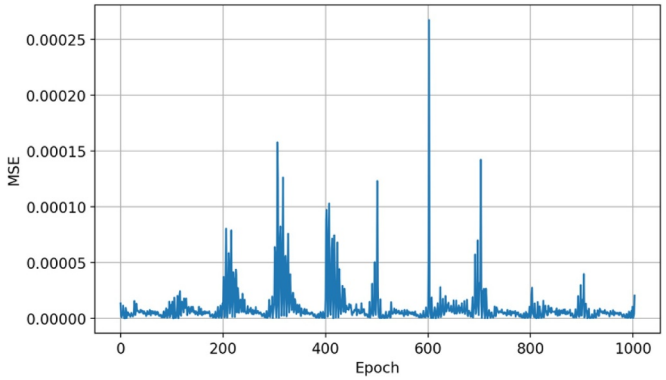

Fig. 21. Training MSE of the BLSTM for 1000 epochs.

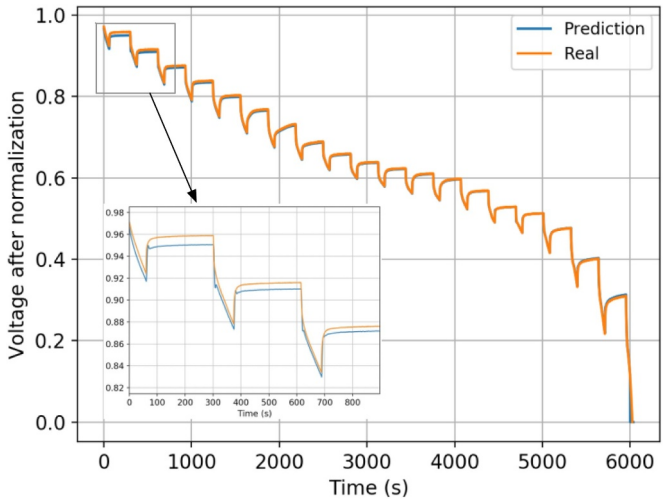

Fig. 22. Comparison of voltage after normalization between the predicted result (proposed study) and the experimental result.

In this study, we propose the use of the GAN-CLS algorithm to generate battery discharge state data and the BLSTM to predict the battery state. Table 1 lists the average time elapsed of 10 generated datasets. Compared with conventional methods, the elapsed time is significantly reduced. Conventional experiments also require the purchase of many batteries for experimental purposes. The proposed methods only require 10 to 30 sets of experimental data to train the networks, resulting in the generation of thousands of pseudo-experimental data; thus, the prediction model will have high precision and generalization performance. Table 2 demonstrates the elapsed time of the training network in each epoch. The internal networks are set to 40 generators cycles and 10 discriminators cycles, the general convergence performance is less than 60 epochs, the total GAN-CLS training time (include CNN preprocess) is less than 750s. The time to generate 120 desired data is ignored because it only takes 100-120ms (with Intel Core i7-9700K Desktop Processor 8 Cores and GeForce RTX 2080Ti Graphics Card), comparing with the experiment modeling time of more than 30000s. Generally, the proposed methods significantly reduce the time cost. The reliability and validity performance are listed in Table 3, with the generated data compared with true data. PCC is the Pearson's correlation coefficient. The generated data is shown to have high similarity.

The modeling processing (include parameters identification and training data collection) is time consuming to the most conventional SOC estimation methods. The experiment run 10 times with 3 different SOH condition batteries, the ten batteries are used in each time. Fig. 18 shows the time cost comparison of experimental modeling and GAN-CLS modeling, the purposed methods have 50 times less time cost than the conventional modeling. Fig. 19 shows the BLSTM methods (include train and prediction time) have 20 times less time cost than the EKF methods. The generated data are normalized to accelerate the rate of convergence of the networks. Using 500 generated datasets in each epoch to train the BLSTM, the tremendous amount data ensures that the MSE is low from the start, as shown in Fig. 20. The training process is conducted for every 12 datasets with the batch of size 60, continuously. Fig. 21 shows the training MSE for 1000 Epochs; the MSE has a distribution caused by the fluctuation of the generated data. Fig. 22 demonstrates that the BLSTM can predict the data with high accuracy.

Each voltage generalization ability in the EKF and proposed approach is compared with a real measured voltage obtained at low (0°C) and high temperatures (50°C) (Fig. 23). According to the comparison among three voltages under 0°C (left figure), it is shown that two methods have a good similar performance on voltage prediction. Unfortunately, the right figure clearly shows the increased voltage prediction errors of two methods under 50°C(0°C⇒50°C), especially the EKF. As previously mentioned in Section 2.1, the EKF significantly depends on the accuracy of model parameters (correct parameter identification) as well as the predetermined noise covariance. Thus, incorrect parameter identification and environmental variables may result in remarkable errors and divergence on battery voltage prediction. As shown in Fig. 23(b), it is not easy to predict the battery voltage in the EKF unless we re-identify the model parameters obtained at 50°C

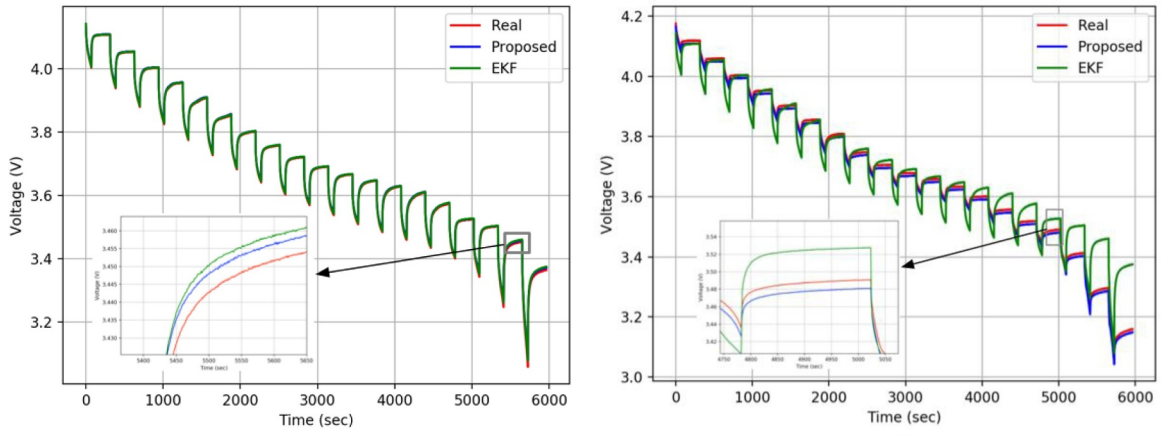

Fig. 23. Voltage generalization ability in the EKF and proposed approach compared with a real measured voltage obtained at low (0°C) and high (50°C) temperatures. (a) Voltage prediction at 0°C, (b) Voltage prediction at 50°C.

and used these values in the EKF. In comparison with real measured voltage at 50°C, the prediction error in the EKF is larger than that of the proposed approach.

The theoretical analysis ensures the validity of the combined methods. The experiment shows that our methods can also generate a corresponding image according to the given SOH. However, there are still some limitations of our method. In some cases, the generated results are not plausible. The generated images have some layers and are not entirely clean. In future work, we will seek solutions to these problems.

5. Conclusions

This paper combines the deep learning technologies of GAN-CLS and BLSTM to estimate the state of batteries. The proposed methods only require a few CNN processed experiment datasets to train the GAN-CLS. The trained networks can generate extremely valid data in contrast to the alternative of running many repeated experiments. The generated data with high PCCs are used to train the BLSTM. The analysis is carried out considering both time cost and error. The time cost results suggest that the GAN-CLS can train and generate data 50 times than experiments, the BLSTM can train and test 20 times than conventional methods. while limitations result from the fluctuation of the networks. The results show a predicted maximum MSE smaller than 0.0025 and the average MSE less than 0.0013. The MSE results suggest that the proposed networks have high accuracy and generalization, and the proposed methods significantly reduce time and material cost

CRediT authorship contribution statement

Haoliang Zhang: Investigation, Writing - original draft. **Wei Tang:** Formal analysis. **Woonki Na:** Methodology, Investigation. **Pyeong-Yeon Lee:** Formal analysis. **Jonghoon Kim:** Writing - review & editing.

Acknowledgements

This material is based upon work supported by the National Science Foundation under Grant No. 1816197.

Supplementary materials

Supplementary material associated with this article can be found, in the online version, at doi:10.1016/j.est.2020.101489.

References

[1] X. Zhang, Y. Wang, J. Wu, Z. Chen, A novel method for lithium-ion battery state of energy and state of power estimation based on multi-time-scale filter, Appl. Energy 216 (2018) 442–451, https://doi.org/10.1016/j.apenergy.2018.02.117.
[2] K. Kutluay, Y. Cadirci, Y.S. Ozkazanc, I. Cadirci, A new online state-of-charge estimation and monitoring system for sealed lead–acid batteries in telecommunication power supplies, IEEE Trans. Ind. Electron. 52 (5) (2005) 1315–1327, https://doi.org/10.1109/tie.2005.855671.
[3] K.S. Ng, C.-S. Moo, Y.-P. Chen, Y.-C. Hsieh, Enhanced coulomb counting method for estimating state-of-charge and state-of-health of lithium-ion batteries, Appl. Energy 86 (9) (2009) 1506–1511, https://doi.org/10.1016/j.apenergy.2008.11.021.
[4] M.R. Khan, G. Mulder, J. Van Mierlo, An online framework for state of charge determination of battery systems using combined system identification approach, J. Power Sources 246 (2014) 629–641, https://doi.org/10.1016/j.jpowsour.2013.07.092.
[5] M. Gholizadeh, F.R. Salmasi, Estimation of state of charge, unknown nonlinearities, and state of health of a lithium-ion battery based on a comprehensive unobservable model, IEEE Trans. Ind. Electron. 61 (3) (2014) 1335–1344, https://doi.org/10.1109/tie.2013.2259779.
[6] C. Truchot, M. Dubarry, B.Y. Liaw, State-of-charge estimation and uncertainty for lithium-ion battery strings, Appl. Energy 119 (2014) 218–227, https://doi.org/10.1016/j.apenergy.2013.12.046.
[7] L. Liu, L.Y. Wang, Z. Chen, C. Wang, F. Lin, H. Wang, Integrated system identification and state-of-charge estimation of battery systems, IEEE Trans. Energy Convers. 28 (1) (2013) 12–23, https://doi.org/10.1109/tec.2012.2223700.
[8] Y. Xing, W. He, M. Pecht, K.L. Tsui, State of charge estimation of lithium-ion batteries using the open-circuit voltage at various ambient temperatures, Appl. Energy 113 (2014) 106–115, https://doi.org/10.1016/j.apenergy.2013.07.008.
[9] S. Sepasi, R. Ghorbani, B.Y. Liaw, Improved extended Kalman filter for state of charge estimation of battery pack, J. Power Sources 255 (2014) 368–376, https://doi.org/10.1016/j.jpowsour.2013.12.093.
[10] M. Mastali, J. Vazquez-Arenas, R. Fraser, M. Fowler, S. Afshar, M. Stevens, Battery state of the charge estimation using Kalman filtering, J. Power Sources 239 (2013) 294–307, https://doi.org/10.1016/j.jpowsour.2013.03.131.
[11] S. Yuan, H. Wu, C. Yin, State of charge estimation using the extended Kalman filter for battery management systems based on the ARX battery model, Energies 6 (1) (2013) 444–470.
[12] C. Zhang, J. Jiang, W. Zhang, S.M. Sharkh, Estimation of state of charge of lithium-ion batteries used in HEV using robust extended Kalman filtering, Energies 5 (4) (2012) 1098–1115, https://doi.org/10.3390/en5041098.
[13] M. Ye, H. Guo, R. Xiong, Q. Yu, A double-scale and adaptive particle filter-based online parameter and state of charge estimation method for lithium-ion batteries, Energy 144 (2018) 789–799, https://doi.org/10.1016/j.energy.2017.12.061.
[14] J. Chen, Q. Ouyang, C. Xu, H. Su, Neural network-based state of charge observer design for lithium-ion batteries, IEEE Trans. Control Syst. Technol. 26 (1) (2018) 313–320, https://doi.org/10.1109/tcst.2017.2664726.
[15] K.T. Chau, K.C. Wu, C.C. Chan, A new battery capacity indicator for lithium-ion battery powered electric vehicles using adaptive neuro-fuzzy inference system, Energy Convers. Manage. 45 (11-12) (2004) 1681–1692.
[16] X. Han, M. Ouyang, L. Lu, J. Li, A comparative study of commercial lithium ion battery cycle life in electric vehicle: capacity loss estimation, J. Power Sources 268 (2014) 658–669, https://doi.org/10.1016/j.jpowsour.2014.06.111.
[17] X. Chen, W. Shen, M. Dai, Z. Cao, J. Jin, A. Kapoor, Robust adaptive sliding-mode observer using RBF neural network for lithium-ion battery state of charge estimation in electric vehicles, IEEE Trans. Veh. Technol. 65 (4) (2016) 1936–1947, https://doi.org/10.1109/tvt.2015.2427659.
[18] W.X. Shen, State of available capacity estimation for lead-acid batteries in electric vehicles using neural network, Energy Convers. Manage. 48 (2) (2007) 433–442, https://doi.org/10.1016/j.enconman.2006.06.023.
[19] S. Rodrigues, N. Munichandraiah, A.K. Shukla, A review of state-of-charge indication of batteries by means of a.c. impedance measurements, J. Power Sources 87 (1–2) (2000) 12–20, https://doi.org/10.1016/s0378-7753(99)00351-1.
[20] H. Blanke, O. Bohlen, S. Buller, R.W. De Doncker, B. Fricke, A. Hammouche, D.U. Sauer, Impedance measurements on lead–acid batteries for state-of-charge, state-of-health and cranking capability prognosis in electric and hybrid electric vehicles, J. Power Sources 144 (2) (2005) 418–425, https://doi.org/10.1016/j.jpowsour.2004.10.028.
[21] W.X. Shen, State of available capacity estimation for lead-acid batteries in electric vehicles using neural network, Energy Convers. Manage. 48 (2) (2007) 433–442.
[22] W.X. Shen, K.T. Chau, C.C. Chan, E.W. Lo, Neural network-based residual capacity indicator for nickel-metal hydride batteries in electric vehicles, IEEE Trans. Veh. Technol. 54 (5) (2005) 1705–1712.
[23] Z. Chen, C. Jiang, Building occupancy modeling using generative adversarial network, Energy Build. 174 (2018) 372–379.
[24] L. Xu, C. Li, X. Xie, G. Zhang, Long-short-term memory network based hybrid model for short-term electrical load forecasting, Information 9 (7) (2018) 165, https://doi.org/10.3390/info9070165.
[25] C.R. Brydges, G.E. Gignac, U.K.H. Ecker, Working memory capacity, short-term memory capacity, and the continued influence effect: a latent-variable analysis, Intelligence 69 (2018) 117–122, https://doi.org/10.1016/j.intell.2018.03.009.
[26] H. Zhang, W. Na, J. Kim, State-of-charge estimation of the lithium-ion battery using neural network based on an improved thevenin circuit model, 2018 IEEE Transportation Electrification Conference and Expo (ITEC), IEEE, 2018, , https://doi.org/10.1109/itec.2018.8450162.
[27] I. Goodfellow, J. Pouget-Abadie, M. Mirza, B. Xu, D. Warde-Farley, S. Ozair, Y. Bengio, Generative adversarial nets, Adv. Neural Inf. Process. Syst. (2014) 2672–2680.
[28] L. Karacan, A. Erdem, E. Erdem, Alpha matting with KL-divergence-based sparse sampling, IEEE Trans. Image Process. 26 (9) (2017) 4523–4536, https://doi.org/10.1109/tip.2017.2718664.
[29] S. Hochreiter, J. Schmidhuber, Long short-term memory, Neural Comput. 9 (8) (1997) 1735–1780, https://doi.org/10.1162/neco.1997.9.8.1735.
[30] M. Arjovsky, S. Chintala, L.. Bottou, Wasserstein generative adversarial networks, Proceedings of the 34th International Conference on Machine Learning, in PMLR, 70 2017, pp. 214–223.